HHS Public Access

Author manuscript

J Magn Reson. Author manuscript; available in PMC 2016 May 01.

Published in final edited form as:

J Magn Reson. 2015 May ; 254: 56–61. doi:10.1016/j.jmr.2015.02.012.

Comparison of Pulse Sequences for R_1–based Electron Paramagnetic Resonance Oxygen Imaging

Boris Epel[a,b] and **Howard J. Halpern**[a]

[a]Department of Radiation and Cellular Oncology, Center for EPR Imaging *in Vivo* Physiology, The University of Chicago, Chicago, IL 60637, USA

[b]Visiting Professor, Department of Physics, Kazan Federal University, Kazan, 420044, Russia

Abstract

Electron paramagnetic resonance (EPR) spin-lattice relaxation (SLR) oxygen imaging has proven to be an indispensable tool for assessing oxygen partial pressure in live animals. EPR oxygen images show remarkable oxygen accuracy when combined with high precision and spatial resolution. Developing more effective means for obtaining SLR rates is of great practical, biological and medical importance. In this work we compared different pulse EPR imaging protocols and pulse sequences to establish advantages and areas of applicability for each method. Tests were performed using phantoms containing spin probes with oxygen concentrations relevant to *in vivo* oxymetry. We have found that for small animal size objects the inversion recovery sequence combined with the filtered backprojection reconstruction method delivers the best accuracy and precision. For large animals, in which large radio frequency energy deposition might be critical, free induction decay and three pulse stimulated echo sequences might find better practical usage.

Keywords

EPR; Imaging; Relaxation; Pulse sequence

1. Introduction

Imaging oxygen in the tissues of living animals and eventually in humans has profound health related consequence. Of the causes of human death worldwide, the four leading causes result from local tissue oxygen starvation. In first world countries seven of the

Corresponding author: Boris Epel, Ph.D. Center for EPR Imaging *in Vivo* Physiology, The University of Chicago, Department of Radiation and Cellular Oncology, MC1105, Rm: ESB-05, 5841 S. Maryland Avenue, Chicago, IL 60637, USA. bepel@uchicago.edu; Tel. +1(773)834-1938; Fax: +1(773)702-5940..

Howard Halpern, M.D., Ph.D.

Center for EPR Imaging *in Vivo* Physiology, The University of Chicago, Department of Radiation and Cellular Oncology, MC1105, Rm: ESB-05, 5841 S. Maryland Avenue, Chicago, IL 60637, USA. h-halpern@uchicago.edu; Tel. +1(773)702-6871; Fax: +1(773)702-5940.

leading causes are from local tissue oxygen starvation. [1] The value of oxygen images increases as their ability to absolutely quantify the average local pO_2 in image voxels increases. More accurate pO_2 quantification allows repeated image to be obtained with more highly resolved pO_2 changes in local tissue. [2] EPR oxygen measurements and images have until recently relied on the increase in transverse relaxation rates ($R_2=1/T_2$, where T_2 is the relaxation time) through Heisenberg spin exchange. [3-6] Since our very early *in vivo* oxygen image [7], a number of groups have published important contributions using EPR imaging including pulse imaging. [8-11] Recently we demonstrated that spin-lattice relaxation (SLR or R_1) based electron paramagnetic resonance (EPR) oxygen images that use soluble spin probes are superior to their phase relaxation based analogs [12]. Spin probe relaxation rates are linearly related to the oxygen tension of molecular oxygen when dissolved in the same solution. This facilitates high precision measurements and imaging of the oxygen tension in live animal tissues [13]. Although the SLR rates of typical spin probes are similar to phase relaxation rates, they carry much less dependence on other factors such as salinity and, especially, spin probe concentration self-relaxation or broadening. This property of SLR imaging makes it possible to obtain nearly absolute oxygen images, greatly advancing the field of *in vivo* oximetry.

A number of approaches to oxygen imaging are possible. The development of trityl spin probes with multi-microsecond relaxation times has enabled *in vivo* EPR oxygen images using pulse techniques, pioneered by the Biophysical Spectroscopy group at the National Cancer Institute[10, 14] and further pursued in our laboratory. [11, 15] More traditional spectral spatial images [16, 17] will not be discussed here. In this paper we examine different R_1 imaging methods.

2. Pulse sequences and Imaging Methods

At present, the two major methodologies for pulse EPR *in vivo* imaging are: electron spin echo (ESE) imaging and single point imaging (SPI). Both account for the instrumental limitations imposed by microsecond-long spin probe electron relaxation times: the imager's dead time as compared with the life time of the signal and static gradients of the magnetic field.

Similarly to MRI [18], it is convenient to discuss pulse EPR imaging methodologies in terms of k-space, the complimentary Fourier space of the image. Every point of the EPR time domain signal at time t can be directly mapped into k-space using the simple relation $\mathbf{k}=\gamma\mathbf{G}t$, where $\mathbf{G}$ is the three- dimensional vector of the static magnetic field gradient and γ is the electron gyromagnetic ratio. Three dimensional uniform image acquisition requires k-values to be sampled on a cube defined by the vertices $(-k_{max}, +k_{max})$, where k_{max} is defined by the target image resolution.

ESE imaging utilizes the complete time trace of spin echo from the end of spectrometer dead time until time t_{max} corresponding to k_{max}. The maximum value of the echo (echo time, t = 0) corresponds to k=0. The value of $|\mathbf{G}|$ is chosen to have a sufficient signal at time t_{max}. The single time trace radially crosses k-space, passing the center of the k-coordinates at the echo time. Typically, the same gradient strength $|\mathbf{G}|$ is chosen for every acquisition, while the

direction of the gradient vector is varied to cover the complete space. The implementation of the gradient sampling algorithm used here has two nested cycles, one for the polar and one for the azimuthal angle of the gradient. The angles are chosen to keep gradient vectors uniformly distributed on the unit sphere. To avoid image artifacts, signals at and around $\mathbf{k} = 0$ ($t = 0$) should be acquired. This precludes the use of free induction decays where the $t = 0$ signal is buried in the dead time of the imager and requires the use of spin-echo sequences [11, 15]. ESE images in our laboratory are reconstructed using filtered backprojection (FBP) algorithms in a spatial domain. This means that time traces are Fourier transformed into a spatial domain prior to reconstruction. The major advantage of ESE imaging is its highly efficient use of data. As a result, most of the acquired echo time trace can be used. Unfortunately, the resulting k-space density sampling does not show optimum results. The samples are very dense around the center of k-space but sparse on the periphery. This complicates image reconstruction and is a source of image artifacts.

The SPI method is based on a different principle. A single point at time $t = \tau$ on the time trace is used to obtain a single k-space value $\mathbf{k_{ijk}}=\gamma\mathbf{G_{ijk}}\tau$ [14, 19, 20]. A different gradient vector $\mathbf{G_{ijk}}$ is selected for the acquisition of each k-space point. Naturally, the dead time of the imager has no effect on the SPI as any acquisition time τ can be chosen. Using the SPI method, no back projection is required and k-space can be sampled in any direction desired, although a rectangular grid is usually chosen. Data acquisition requires three nested loops, one for each Cartesian coordinate. The data taken along each Cartesian direction forms a pseudo-echo. The final image is obtained by a three dimensional Fourier transformation of these pseudo-echos. More sophisticated methods for k-space sampling were described elsewhere [21]. These can reduce the acquisition burden imposed by the necessity to acquire the number of time traces equal to the number of voxels in the resulting image.

Both ESE and SPI methodologies provide high quality EPR images of relaxation times and are used for tissue oxymetry. Both methodologies can also be used to determine R_1 (SLR). We examined three conventional pulse sequences to determine R_1 [22] combined with these methodologies:

- Inversion recovery (IRESE and IRSPI)
- Stimulated echo (SE, ESE methodology only)
- Saturation by fast repetition (SFR ESE and SFR SPI)

The first type of R_1 sequence, inversion recovery (Figs. 1A and 1B), inverts spin polarization by using a broadband π pulse. The recovery is measured as a function of the delay, T, after the inversion pulse (Fig. 2A). IRESE was used in our earlier publication [12]. The proportionality coefficient A in Fig. 2A, less than or equal to two, accounts for the incomplete inversion which may be due to RF field inhomogeneity in the resonator and the limited bandwidth of the inversion pulse. The delay τ (Fig. 1A) is fixed with a minimum value limited by the dead time of the imager. The bandwidth of the echo detected inversion recovery sequence with ESE detection, IRESE (Fig. 1A), is approximately equal to the bandwidth of the two-pulse ESE detection sequence. The inversion recovery sequence for SPI, referred to as IRSPI, utilizes FID detection (Fig. 1B). The bandwidth of this sequence is equal to that of a single RF pulse.

The second sequence, SE (Fig. 1C), is the three-pulse 'stimulated' echo sequence. In this sequence the π pulse of the two-pulse ESE experiment is split into two π/2 pulses separated by a time T. After the first two π/2 pulses, the magnetization is stored along the z-axis (longitudinal axis) . Different delays T probe the magnetization decay. The third π/2 pulse rotates the z-component back into the transverse xy-plane where it gives rise to a stimulated echo at fixed time τ after the third pulse. The amplitude of the SE signal decays as T increases, as shown in Figure 2B. This sequence has nearly twice the bandwidth of the two-pulse ESE (and thus also the IRESE) sequence with the same RF pulse length [23]. By applying longer RF pulses with the same overall sequence bandwidth the applied power can be reduced, thereby also reducing the specific absorption rate (SAR) in living subjects. This factor may be crucial to human applications.

In the SFR experiment (Figs. 1D and 1E) the amplitude of the ESE or FID is measured as a function of repetition time, T_R, for the respective sequence. As the repetition rate increases, the signal from the spin system saturates thus allowing the measurement of R_1 (Fig. 2C).

We present a study of these R_1 imaging methods using our 250 MHz pulse spectrometer [15].

3. Results

Spatial images obtained using ESE and SPI methodologies, are presented in Figures 3B and 3C, respectively. Bottle phantoms with narrow line trityl OX063H radical were used [24]. The phantoms were placed in the resonator at an angle to the horizontal plane, as shown in Figure 3A. Figure 4 displays selected R_1 images. The ESE and SPI images are very similar. In the figure, the SPI image appears slightly larger due to better SPI performance in the fringe field of the resonator. The results of R_1 imaging of two phantoms with 0% and 9.3% of O_2 (71 torr pO_2 at physiologic temperature and atmospheric pressure) respectively are summarized in Table 3. This range of oxygen concentrations is relevant to hypoxia studies of animals [25-27]. The average across phantom relaxation times, as determined under non-imaging conditions, is given for comparison. IRESE and SE pulse sequences with a large number of steps along T and long accumulation times were used. The SE sequence slightly overestimated R_1 when compared to the inversion recovery sequence, probably due to the effect of spectral diffusion on relaxation time [22, 28]. The standard deviation of relaxation times for all voxels of homogeneous phantoms was used to estimate errors. Of all the ESE R_1 imaging methods, the IRESE sequence demonstrated the smallest standard deviation, 4% of the absolute value for 0% O_2 and 12% of the absolute value for 9.3% O_2. SE showed a slightly worse performance, with a standard deviation of 5% of the absolute value for 0% O_2 and 17% for 9.3% O_2. For the 0% O_2 phantom the SFR methods demonstrated large standard deviations. For the 9.3% O_2 phantom the SFR methods were unable to produce an R_1 image because R_1 was too fast to become saturated by the highest repetition rate our power amplifier can achieve (~7% duty cycle). As with the ESE sequences, the IRSPI sequence demonstrated much better performance (6% and 14% for 0% O_2 and 9.3% O_2, respectively) than the SFR SPI, but a slightly worse performance than IRESE.

For all studied sequences the R_1 errors were growing faster than R_1 itself. Many experimental and instrumental settings may lead to this result. The dead time of the imager defines the shortest acquisition delay (630 ns in this study). For the ESE sequence, the attenuation of the signal at this delay is ~23% for the hypoxic sample and more than 60% for 9.3% O_2 sample. This explains a factor of 2 difference in imaging errors. In addition, the delay times in pulse sequences were optimized to capture both high and low R_1. This again favored the measurement precision for slow relaxation rates as the sequences with long delays generated no signal for 9.3% O_2 sample.

4. Discussion

Since the imaging parameters for each type of image were chosen in order to produce similar spatial resolution, only the relaxation time accuracy needed to be considered as a figure of merit. A major factor affecting image accuracy is the signal to noise ratio (SNR). Assuming that for each methodology the imager noise characteristics are the same, the image SNR will be governed by the amplitude of the signal, the effect of SLR on this signal and the number of signal acquisitions per unit of time (acquisition rate). Inversion recovery has the greatest SLR effect on the signal; it is double that of other sequences, since the evolution of the signal from negative to positive is monitored. The amplitude of the SLR effect for SFR is proportional to $\exp(-R_1 * T_R^{MIN})$, where T_R^{MIN} is the shortest T_R in an experiment. In our instrument, T_R^{MIN} was governed by the duty cycle of the power amplifier. For 9.3% O2 phantom, the imager did not produce sequences with a T_R low enough to cause a substantial saturation effect on the echo or FID amplitude. This eliminated the feasibility of using SFR imaging for our instrument. The performance of the SE method is worse than that of IRESE both because the echo amplitude is decreased by a factor of two [23] and because of the lower SLR effect on the echo amplitude. The SPI image SNR is lower than that of ESE since only one point of the time domain signal was used. However, when correctly estimating relaxation times in the absence of reconstruction artifacts, the SPI may become less dependent on the SNR [14, 19]. Accordingly, Table 3 demonstrates the advantage of IRESE over all SLR sequences, while SE and IRSPI show a similar, but slightly lower, performance.

Experimental advantages, however, can be gained from the considerably smaller power requirements of the SE and IRSPI sequences (Table 2). Of all the echo-based imaging methods, the SE images (which require a power amplifier with only $1/25^{th}$ of peak power), demand the least peak power and the lowest average power for the same bandwidth. The power required for RF pulses with identical B_1 increases proportionally with the resonator volume. Applying SLR imaging to larger animals may require larger resonators and more power than currently available sources can deliver. Thus the lower RF power requirements may make SE and IRSPI sequences attractive for large subject imaging. The lower average power deposition may also make these sequences favorable for human applications.

5. Conclusions

This work demonstrates that in the absence of power deposition restrictions, an inversion recovery sequence combined with the filtered backprojection reconstruction method delivers

the best R_1 and pO_2 accuracy and precision. For large animals, where minimization of radio frequency energy deposition might be critical, free induction decay single point imaging and three pulse echo filtered backprojection imaging might find better practical usage.

6. Materials and Methods

6.1 Spin probe

The spin probe used for the EPR imaging was the trityl OX063 radical methyl-tris[8-carboxy-2,2,6,6-tetrakis[2-hydroxyethyl]benzo[1,2-d:4,5-d']bis[1,3]dithiol-4-yl]-trisodium salt, molecular weight = 1,427 from GE Healthcare (Little Chalfont, Buckinghamshire, UK). Phantoms containing 1 mM solution of spin probe in normal saline (0.90% w/v of NaCl) were fabricated from Wheaton vials, flat-bottomed borosilicate glass cylinders with a 9.5 mm inner diameter and 45 mm length. The 0% O_2 sample was deoxygenated using a multiple-cycle freeze-pump-thaw technique and flame sealed. The 9.3% O_2 sample was produced by bubbling the solution with a nitrogen-oxygen gas mixture and then sealing with epoxy.

6.2 Pulse imager and details of measurements

A versatile pulse 250 MHz imager was used to produce the images shown here, as has been described in detail elsewhere [15, 29]. A pulse amplitude modulation switch was added to produce π/2- and π- pulses of equal duration [30]. The maximum achieved duty cycle of the 2 kW BT-2000 (TOMCO, Australia) power amplifier was 7%. This included 325 ns pre-gating for each RF pulse. The duty cycle was the factor that limited repetition rates in SFR ESE and SFR SPI experiments. The imager control software SpecMan4EPR version 1.1.6 [31] was used.

Pulse power optimization—Loop gap resonators may have a substantial non uniformity of the RF magnetic field. This results in different electron spin turning angles at different positions in the resonator. For the images we used RF powers that maximized the overall EPR signal from the phantom. This choice of power may have led to reduced SNR of certain phantom areas experiencing lower and higher than optimum turning angles.

Bandwidth measurements—Sequence bandwidths were measured using methodology presented elsewhere [15]. The amplitude of a narrow line EPR signal in the absence of gradients was plotted as a function of the homogeneous magnetic field. The frequency of the EPR signal, in this case, is different from the base frequency of the imager. This creates the ability to probe the frequency domain transfer function. This transfer function has contributions from the resonator, imager hardware and pulse sequence. The bandwidth is given at the EPR signal amplitude 3 dB point [15].

Pulse sequence parameters—The range of pulse sequence parameters was optimized for the given spin probe and instrumental capabilities. The minimum T in SE and IRESE were chosen as the shortest values that produced undisturbed echo traces. The 4-step, 16-step and 64-step CYCLOPS were used for FID, IRESE and SE sequences, respectively.

Applied RF power—RF power was calculated using the formulae $P = \Sigma t_i P_i / T_R$, where t_i and P_i are the durations and powers of each pulse in the sequence respectively. T_R is the repetition time. T_R is the duration between first pulses of consecutive pulse sequences. For images where T_R was changed during imaging, the applied power was averaged over all pulse sequences. Most of the RF power was deposited into the resonator resistive load (shunt resistor). Based on the comparison of loaded and unloaded resonator quality factors of about 1 per cent, the power deposition into the sample is expected to be below 10% of the applied power.

6.3 Image parameters

To facilitate the image quality comparison, image acquisition time was fixed at 10 minutes. The settings for SPI and ESE images were chosen to have spatial resolution equal to 1.5 mm. Tables 1 and 2 present the parameters of the SLR sequences. The repetition time for ESE sequences, T_R, was adjusted to keep constant the delay between the last pulse in one sequence and the first pulse, T^{LF}_R, of the next one. This repetition time definition allows longitudinal magnetization after the last pulse to relax equally for sequences of different durations. This method is more efficient than the conventional method in which the repetition time in the experiment is kept constant, independent of echo time and sequence length. The optimal repetition time in phantom experiments was determined as the shortest T_R for which the sequence still provided correct R_1 values. For correct determination of R_1 in inversion recovery experiments, the image recorded at a very long, essentially infinite, time T is very important. This image, however, is identical to the image recorded without an inversion pulse, which may be acquired in a shorter time. Thus in IRESE/IRSPI images, the image with T = 40 μs was replaced by an image obtained without an inversion pulse.

For all FBP images the same three-dimensional protocol [15, 32] was applied: 208 projections corresponding to an 18x18 equal solid angle gradient spacing [33] were acquired; gradient strength was $|\vec{G}|$ mT/m; object field of view was 4.24 cm. A baseline (acquisition at 1.5 mT lower field) acquired every fourth trace (53 traces in all). To reduce FBP reconstruction artifacts, the acquired set of projections was linearly interpolated four-fold [34] and filtered with a 3D Ram-Lak filter with a cutoff at one-half of the Nyquist frequency. In the images we kept only those voxels with signal amplitude greater than 15% of the maximum amplitude at the shortest delay. Standard deviation of the relaxation rates in a homogeneous phantom was used as an estimation of relaxation rate errors. Two outer layers of images were excluded from standard deviation calculations to avoid partial volume averaging artifacts. Further data acquisition and processing methods are discussed in detail elsewhere [15].

The SPI protocol involved the acquisition of FIDs at a fixed delay, t_{SPI} (Table 1), with gradients corresponding to a 23×23×23 matrix (from -15 mT/m to +15 mT/m) in which only the gradients $|G| \leq 15$ mT/m were acquired. A baseline was acquired every 20th trace to suppress imager related artifacts. The 3D ‘pseudo-echo’ matrix was zero filled to a 69×69×69 matrix and Fourier transformed to produce the final image.

All data processing was performed using in-house software written in MATLAB (The Mathworks, Inc., and Natick, MA, USA).

6.4 Non-imaging vs. imaging conditions

Acquisition of imaging information requires considerable time. Therefore imaging protocols have to balance measurement precision with the duration of the experiment. As a result, the relaxation times in imaging protocols are estimated from only eight points on the decay curve. Such restrictions do not apply for non-imaging measurements on phantoms, which have more numerous (80 vs 8 for imaging) delays of a wider range (more than 2 times wider than for imaging).

Acknowledgements

We acknowledge our colleagues from the Center for EPR Imaging *In vivo* Physiology and NIH grants P41EB002034 and CA98575. BE acknowledges partial support provided by the Program of Competitive Growth, Kazan Federal University.

References

1. Longo, DL.; Fauci, AS.; Kasper, DL.; Hauser, SL.; Jameson, JL.; Loscalzo, J. Harrison's Principles of Internal Medicine. McGraw Hill; New York, NY: 2011. p. 3610ISBN-13: 978-0071802154
2. Braun RD, Lanzen JL, Dewhirst MW. Fourier analysis of fluctuations of oxygen tension and blood flow in R3230Ac tumors and muscle in rats. Am J Physiol. 1999; 277:H551–H568. [PubMed: 10444480]
3. Backer JM, Budker VG, Eremenko SI, Molin YN. Detection of the kinetics of biochemical reactions with oxygen using exchange broadening in the ESR spectra of nitroxide radicals. Biochim Biophys Acta. 1977; 460:152–156. Doi 10.1016/0005-2728(77)90161-X. [PubMed: 192284]
4. Popp CA, Hyde JS. Effects of Oxygen on Electron-Paramagnetic-Resonance of Nitroxide Spin-Label Probes of Model Membranes. J. Magn. Reson. 1981; 43:249–258. Doi 10.1016/0022-2364(81)90036-6.
5. Eastman MP, Kooser RG, Das MR, Freed JH. Studies of Heisenberg Spin Exchange in ESR Spectra. I. Linewidth and Saturation Effects. J Chem Phys. 1969; 51:2690–2709. Doi 10.1063/1.1672395.
6. Molin, YN.; Salikhov, KM.; Zamaraev, KI. Spin Exchange: Principles and Applications in Chemistry and Biology. Springer-Verlag; Berlin: 1980. ISBN 978-3-642-67668-0
7. Halpern HJ, Yu C, Peric M, Barth E, Grdina DJ, Teicher BA. Oxymetry Deep in Tissues with Low-Frequency Electron-Paramagnetic-Resonance. Proc. Natl Acad. Sci. USA. 1994; 91:13047–13051. Doi 10.1073/pnas.91.26.13047. [PubMed: 7809170]
8. Kuppusamy P, Chzhan M, Samouilov A, Wang PH, Zweier JL. Mapping the Spin-Density and Lineshape Distribution of Free-Radicals Using 4d Spectral-Spatial Epr Imaging. Journal of Magnetic Resonance Series B. 1995; 107:116–125. Doi 10.1006/jmrb.1995.1067. [PubMed: 7599947]
9. Krishna MC, Kuppusamy P, Afeworki M, Zweier JL, Cook JA, Subramanian S, Mitchell JB. Development of functional electron paramagnetic resonance imaging. Breast disease. 1998; 10:209–220. [PubMed: 15687576]
10. Murugesan R, Cook JA, Devasahayam N, Afeworki M, Subramanian S, Tschudin R, Larsen JA, Mitchell JB, Russo A, Krishna MC. In vivo imaging of a stable paramagnetic probe by pulsed-radiofrequency electron paramagnetic resonance spectroscopy. Magnet Reson Med. 1997; 38:409–414. Doi 10.1002/mrm.1910380309.
11. Mailer C, Sundramoorthy SV, Pelizzari CA, Halpern HJ. Spin echo spectroscopic electron paramagnetic resonance imaging. Magnet Reson Med. 2006; 55:904–912. Doi 10.1002/Mrm.20849.

12. Epel B, Bowman MK, Mailer C, Halpern HJ. Absolute oxygen R1e imaging in vivo with pulse electron paramagnetic resonance. Magnet Reson Med. 2014; 72:362–368. 10.1002/mrm.24926.
13. Epel B, Halpern HJ. Electron paramagnetic resonance oxygen imaging in vivo., in: Electron Paramagnetic Resonance. The Royal Society of Chemistry. 2013:180–208.
14. Subramanian S, Devasahayam N, Murugesan R, Yamada K, Cook J, Taube A, Mitchell JB, Lohman JAB, Krishna MC. Single-point (constant-time) imaging in radiofrequency Fourier transform electron paramagnetic resonance. Magnet Reson Med. 2002; 48:370–379. Doi 10.1002/Mrm.10199.
15. Epel B, Sundramoorthy SV, Mailer C, Halpern HJ. A versatile high speed 250-MHz pulse imager for biomedical applications. Conc. Magn. Reson. B. 2008; 33B:163–176. Doi 10.1002/Cmr.B.20119.
16. Maltempo MM. Differentiation of Spectral and Spatial Components in Electron-Paramagnetic-Res Imaging Using 2-D Image-Reconstruction Algorithms. J. Magn. Reson. 1986; 69:156–161. Doi 10.1016/0022-2364(86)90229-5.
17. Maltempo MM, Eaton SS, Eaton GR. Spectral-Spatial Two-Dimensional EPR Imaging. J. Magn. Reson. 1987; 72:449–455. Doi 10.1016/0022-2364(87)90149-1.
18. Twieg DB. The k-trajectory formulation of the NMR imaging process with applications in analysis and synthesis of imaging methods. Medical Physics. 1983; 10:610–621. Doi 10.1118/1.595331. [PubMed: 6646065]
19. Matsumoto K, Subramanian S, Devasahayam N, Aravalluvan T, Murugesan R, Cook JA, Mitchell JB, Krishna MC. Electron paramagnetic resonance imaging of tumor hypoxia: Enhanced spatial and temporal resolution for in vivo pO(2) determination. Magnet Reson Med. 2006; 55:1157–1163. Doi 10.1002/Mrm.20872.
20. Devasahayam N, Subramanian S, Murugesan R, Hyodo F, Matsumoto KI, Mitchell JB, Krishna MC. Strategies for improved temporal and spectral resolution in in vivo oximetric imaging using time-domain EPR. Magnet Reson Med. 2007; 57:776–783. Doi 10.1002/Mrm.21194.
21. Subramanian S, Chandramouli GVR, McMillan A, Gullapalli RP, Devasahayam N, Mitchell JB, Matsumoto S, Krishna MC. Evaluation of partial k-space strategies to speed up time-domain EPR imaging. Magnet Reson Med. 2013; 70:745–753. Doi 10.1002/Mrm.24508.
22. Schweiger, A.; Jeschke, G. Principles of Pulse Electron Paramagnetic Resonance. Oxford University Press; 2001. DOI: 10.1002/jctb.936
23. Bowman, MK. Modern Pulsed and Continuous Electron Spin Resonance. Wiley & Sons; 1990. Fourier Transform Electron Spin Resonance; p. 1-42.ISBN: 978-0-471-50274-6
24. Ardenkjaer-Larsen JH, Laursen I, Leunbach I, Ehnholm G, Wistrand LG, Petersson JS, Golman K. EPR and DNP properties of certain novel single electron contrast agents intended for oximetric imaging. J. Magn. Reson. 1998; 133:1–12. Doi 10.1006/jmre.1998.1438. [PubMed: 9654463]
25. Elas M, Williams BB, Parasca A, Mailer C, Pelizzari CA, Lewis MA, River JN, Karczmar GS, Barth ED, Halpern HJ. Quantitative tumor oxymetric images from 4D electron paramagnetic resonance imaging (EPRI): Methodology and comparison with blood oxygen level-dependent (BOLD) MRI. Magnet Reson Med. 2003; 49:682–691. DOI: 10.1002/mrm.10408.
26. Elas M, Bell R, Hleihel D, Barth ED, Mcfaul C, Haney CR, Bielanska J, Pustelny K, Ahn KH, Pelizzari CA, Kocherginsky M, Halpern HJ. Electron paramagnetic resonance oxygen image hypoxic fraction plus radiation dose strongly correlates with tumor cure in FSA fibrosarcomas. International Journal of Radiation Oncology Biology Physics. 2008; 71:542–549. DOI 10.1016/j.ijrobp.2008.02.022.
27. Matsumoto S, Espey MG, Utsumi H, Devasahayam N, Matsumoto KI, Matsumoto A, Hirata H, Wink DA, Kuppusamy P, Subramanian S, Mitchell JB, Krishna MC. Dynamic monitoring of localized tumor oxygenation changes using RF pulsed electron paramagnetic resonance in conscious mice. Magnet Reson Med. 2008; 59:619–625. Doi 10.1002/Mrm.21500.
28. Eaton, SS.; Eaton, GR. Biological Magnetic Resonance. Kluwer Academic/Plenum Publishers; New York: 2000. Relaxation Times of Organic Radicals and Transition Metal Ions. ISBN 978-0-306-47109-4

29. Sundramoorthy SV, Epel B, Mailer C, Halpern HJ. A Passive Dual-Circulator Based Transmit/Receive Switch for Use with Reflection Resonators in Pulse Electron Paramagnetic Resonance. Conc. Magn. Reson. B. 2009; 35B:133–138. Doi 10.1002/Cmr.B.20141.

30. Quine RW, Tseytlin M, Eaton SS, Eaton GR. A Very Fast Switched-Attenuator Circuit for Microwave and RF Applications. Conc. Magn. Reson. B. 2010; 37B:39–44. Doi 10.1002/Cmr.B.20157.

31. Epel B, Gromov I, Stoll S, Schweiger A, Goldfarb D. Spectrometer manager: A versatile control software for pulse EPR spectrometers. Conc. Magn. Reson. B. 2005; 26B:36–45. Doi 10.1002/cmr.b.20037.

32. Eaton, GR.; Eaton, SS.; Ohno, K. EPR Imaging and in vivo EPR. CRC Press; Boca Raton FL: 1991. ISBN-13: 000-0849349230

33. Ahn KH, Halpern HJ. Spatially uniform sampling in 4-D EPR spectral-spatial imaging. J. Magn. Reson. 2007; 185:152–158. DOI 10.1016/j.jmr.2006.12.007. [PubMed: 17197215]

34. Ahn KH, Halpern HJ. Comparison of local and global angular interpolation applied to spectral-spatial EPR image reconstruction. Medical Physics. 2007; 34:1047–1052. Doi 10.1118/1.2514090. [PubMed: 17441251]

Highlights

1. A variety of pulse sequences can be used for pulse EPR imaging
2. Inversion recovery sequences deliver best accuracy and precision
3. Free induction decay and three pulse echo sequences show less average power deposition

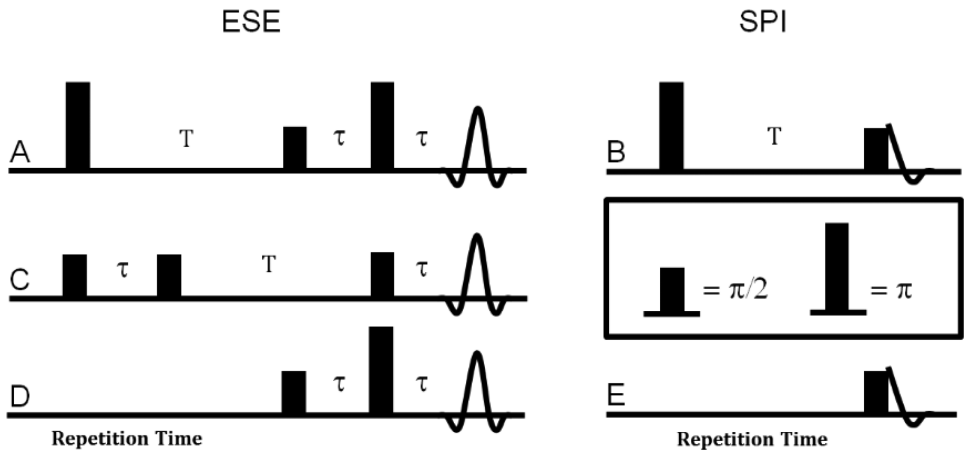

Figure 1.

Pulse sequences for R_1 measurements: A. IRESE; B. IRSPI; C. SE; D. SFR FBP; E. SFR SPI.

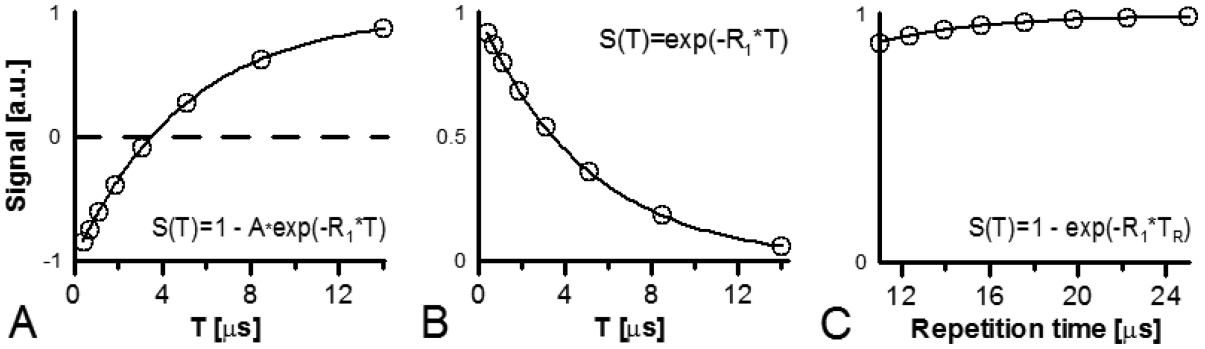

Figure 2.

The simulation of a single voxel's signal amplitude dependence: A. on T in inversion recovery experiments; B. on T in stimulated echo experiments; and C. on repetition time T_R in saturation by fast repetition experiments. The simulated signals are normalized to 1. R_1 equal to $200 \cdot 10^3$ s^{-1} was used for simulation.

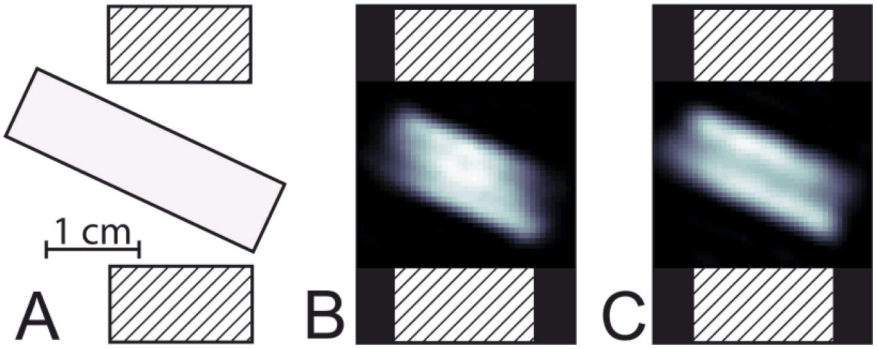

Figure 3.

A. Schematic drawing of a glass tube containing the spin probe in the 19 mm loop-gap resonator. Axial cut of the resonator is shown. The patterned elements represent resonator structures. B and C. The slices (~ 0.7 mm thickness) in the vertical plane of the EPR intensity images of 0% O_2 phantom were obtained using ESE and SPI, respectively. The resonator structure is superimposed on the images for presentation purposes.

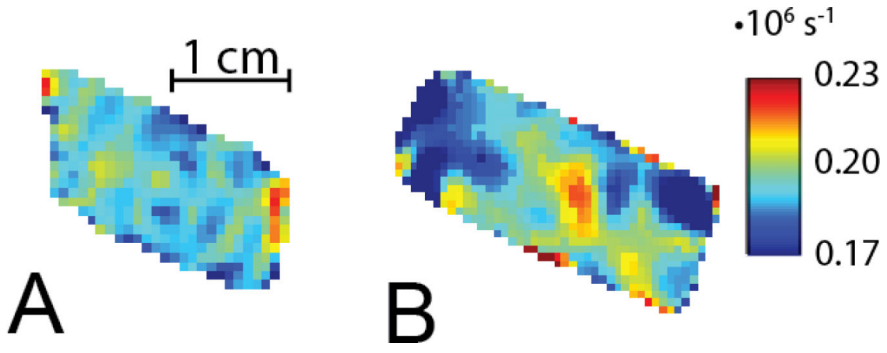

Figure 4.

The slices (~ 0.7 mm thickness) in the vertical plane of R_1 images of 0% O_2 phantom obtained using A. IRESE and B. IRSPI.

Table 1

Pulse sequences and imaging protocols.

Protocol	Description
Non-imaging conditions IRESE	π-T-π/2-τ-π-τ-echo; 35 ns π/2 and π RF pulses; τ = 630 ns; 16-step phase cycling for detection sequence; 80 T's logarithmically spaced between 0.5 μs and 32 μs; 80 μs repetition time; echo is integrated; T's are measured in random order.
Non-imaging conditions SE	π/2-τ-π/2-T-π/2- τ -echo; 60 ns RF pulses; τ = 600 ns; 32-step phase cycling; 80 T's logarithmically spaced between 0.5 μs and 32 μs; 80 μs repetition time; echo is integrated; T's are measured in random order.
IRESE imaging	π-T-π/2-τ-π-τ-echo; 35 ns π/2 and π RF pulses; time trace 1500 points with 4 ns dwell time; τ = 630 ns; 16-step phase cycling applied only for detection sequence, 9600 acquisitions per T, including phase cycling; 8 T's logarithmically spaced between 0.41 μs and 14 μs; TLFR = 25 μs (see Section 6.3 for the definition); |**G**|=15 mT/m; imaging time 10 minutes.
SE imaging	π/2-τ-π/2-T-π/2- τ -echo; 75 ns RF pulses; time trace 1500 points with 4 ns dwell time; τ = 550 ns; 16-step phase cycling, 12160 acquisitions per T, including phase cycling; 8 T's logarithmically spaced between 0.44 μs and 14 μs; TLFR = 25 μs; |**G**|=15 mT/m; imaging time 10 minutes.
SFR imaging	π/2-τ-π/-τ-echo; 35 ns π/2 and π RF pulses; time trace 1500 points with 4 ns dwell time; τ = 630 ns; 16-step phase cycling, 16800 echoes, including phase cycling; 8 images with different repetition times logarithmically spaced between 10 μs (the shortest achieved) and 25 μs; |**G**|=15 mT/m; imaging time 10 minutes.
IRSPI imaging	π-T-π/2-FID; 75 ns π/2- and 150 ns π-RF pulse; t_{SPI} = 790 ns; GMAX=15 mT/m; 4-step phase cycling applied only for detection sequence, 420 acquisitions per T, including phase cycling; 8 T's logarithmically spaced between 0.41 μs and 14 μs; TLFR = 25 μs; imaging time 10 minutes.
SFR SPI imaging	π/2-FID; 80 ns π/2 RF pulse; t_{SPI} = 790 ns; GMAX=15 mT/m; 4-step phase cycling, 720 fid's, including phase cycling; 8 images with different repetition times logarithmically spaced between 9 μs and 25 μs; imaging time 10 minutes.

Table 2

Pulse sequence parameters

Pulse Sequence	Pulse length	RF power [W]	Bandwidth [MHz]	Transmitted Average Power [W]
IRESE	35 ns, π/2 and π	39.6 (π/2), 158.5 (π)	8.7	0.42
SE	75 ns, π/2	6.3 (π/2)	8.8	0.05
SFR ESE	35 ns, π/2 and π	39.6 (π/2), 158.5 (π)	8.7	0.25
IR SPI	75 ns π/2, 150 ns π	6.3 (π/2 and π)	11.6	0.05
SFR SPI	75 ns, π/2	6.3 (π/2)	11.6	0.03

Table 3

Precision of SLR rate images obtained in 10 minutes on phantom containing 1 mM OX063 dissolved in normal saline.

	0% pO_2			9.3% pO_2		
Pulse Sequence	**Average R_1 [$\cdot 10^3$ s^{-1}]**	**Standard deviation of R_1 [$\cdot 10^3$ s^{-1}]**	**Non imaging R_1 [$\cdot 10^3$ s^{-1}]**	**Average R_1 [$\cdot 10^3$ s^{-1}]**	**Standard deviation of R_1 [$\cdot 10^3$ s^{-1}]**	**Non imaging R_1 [$\cdot 10^3$ s^{-1}]**
IRESE	200	7.9	207	760	89.8	752
SE	233	11.4	227	741	128.5	763
IR SPI	203	11.4		730	100.3	
SFR ESE	196	33.5		N/A*	N/A*	
SFR SPI	330	52.8		N/A*	N/A*	

* the SFR sequences were unable to produce precise measurement.